IEEE Photonics Journal
An IEEE Photonics Society Publication

Open Access

Integrated Wavelength Beam Emitter on Silicon for Two-Dimensional Optical Scanning

Volume 11, Number 6, December 2019

Zhenmin Du
Chengyang Hu
Guiyuan Cao
Han Lin
Baohua Jia
Sigang Yang
Minghua Chen
Hongwei Chen

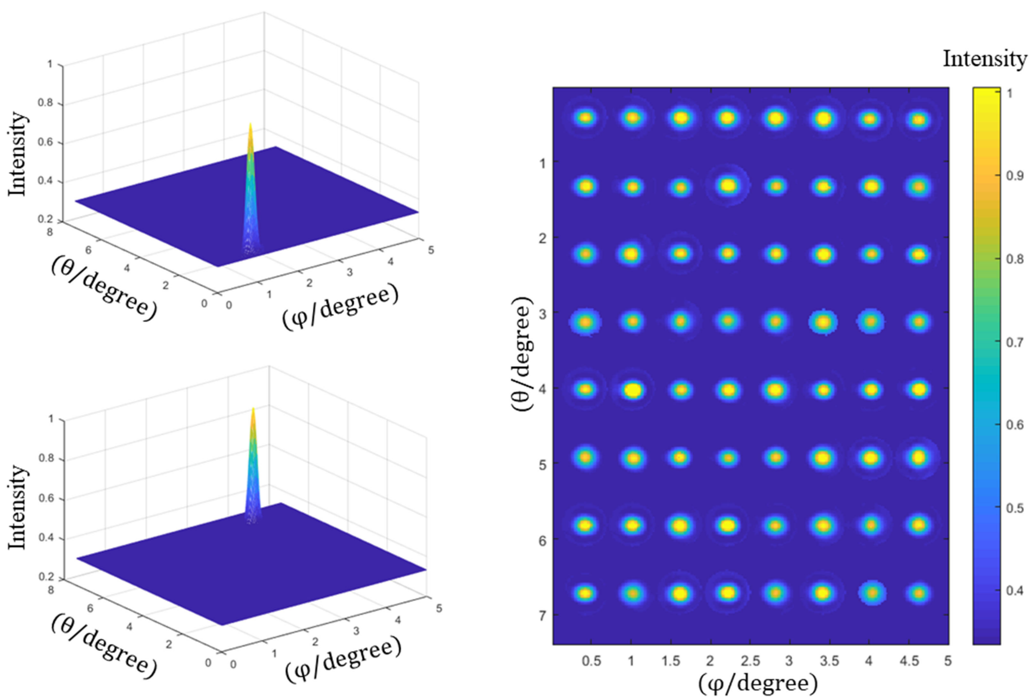

DOI: 10.1109/JPHOT.2019.2943641

IEEE photonics SOCIETY
IEEE

Integrated Wavelength Beam Emitter on Silicon for Two-Dimensional Optical Scanning

Zhenmin Du,[1,2] Chengyang Hu,[1,2] Guiyuan Cao,[3] Han Lin,[3] Baohua Jia ,[3] Sigang Yang ,[1,2] Minghua Chen ,[1,2] and Hongwei Chen [1,2]

[1]Department of Electronic Engineering, Tsinghua University, Beijing 100084, China
[2]Beijing National Research Center for Information Science and Technology (BNRist), Beijing 100084, China
[3]Centre for Translational Atomaterials, Faculty of Engineering, Science and Technology, Swinburne University of Technology, John Street Hawthorn VIC 3122, Australia

DOI:10.1109/JPHOT.2019.2943641

Manuscript received September 9, 2019; accepted September 21, 2019. Date of publication July 25, 2019; date of current version December 13, 2019. This work was supported in part by the NSFC under Contract 61771284, in part by the Beijing Natural Science Foundation under Contract L182043, and in part by the Beijing Municipal Science & Technology Commission under Grant Z181100008918011.
Corresponding author: Hongwei Chen (e-mail: chenhw@tsinghua.edu.cn).

Abstract: A novel integrated on-chip wavelength-based beam emitter is proposed and fabricated to realize two-dimensional optical scanning. By combining both wavelength division filters and emission array, 80×8 far-field optical beam spots are achieved with a field of view of $6^\circ \times 4^\circ$. Both collimation and projection modes are tested and 64 wavelength channels are realized in 10 nm bandwidth from 1550 to 1560 nm. This device can be used for LIDAR, optical wireless communication, and high-speed infrared imaging applications.

Index Terms: Integrated photonics, optical scanner.

1. Introduction

Optical beam scanners have attracted great attention in recent years due to their potential use in a broad range of applications, like high-speed optical communication [1], [2], laser mapping [3] and laser imaging [4]. Traditional optical beam steering systems use electrical motors to scan a laser beam over an area [5], which limit the scanning rate and increase the cost. Integrated photonics provide a path for low-cost and non-mechanical beam steering systems. Silicon photonics, due to its complementary metal–oxide–semiconductor (CMOS) compatibility potentially enable on-chip beam scanners with high volume and low cost [6]. Optical phased arrays (OPAs) using silicon photonics have been proposed as a promising architecture to achieve beam steering [7]–[14]. OPA is generally composed of an array of optical phase shifters and emitters. By tuning the phases of emitters, the emitted light interferes constructively in the far field at certain angles. However, in order to achieve larger angular resolution, the number of antennas and phase shifters will be very huge. In this case, it will be very difficult to increase the space between phase shifters to avoid thermal crosstalk and high power consumption will be an issue at the same time. A 2-dimensional (2D) optical waveguide phased array containing 4096 emitters was developed [15]. Although a total of 4096 emitters are placed in the array, only 64 of them have the corresponding thermo-optic phase shifter. To reduce the complexity of tuning system, some OPAs use wavelength tuning to steer the

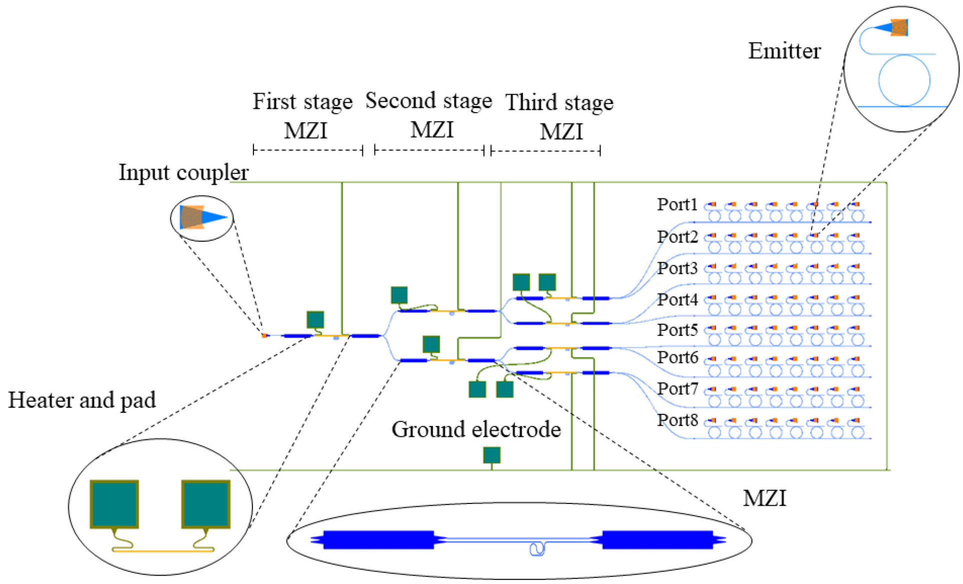

Fig. 1. Structure layout of the device.

second dimension [16], [17] in a simple way or purely use wavelength tuning to steer a beam in 2D [18].

In this paper, a wavelength based 2D beam emitter is realized using a standard silicon photonics fabrication process. The approach to achieve 2D scanning for the device is through wavelength tuning and wavelength-to-space mapping. In this case, a large scanning angle in 10 nm wavelength range can be realized. At the same time, no complicated adjustment system is required during the scanning process to adjust the voltage to achieve phase control. This wavelength-to-space mapping device consists of two main parts, filter module and optical emitter array. Filter module which consists of Mach-Zehnder interferometer(MZI) and micro-rings array is used to divide input light into different wavelength-band and send them to the emitter array. Then the light from different emitters is fed into free space. Thus the optical beam can be scanned by simply changing the input wavelength. Each beam emitted from the device is different in space, time and wavelength domain, which gives the device a lot of advantages that can be exploited. For instance, it can achieve variable scanning rate and can realize arbitrary spatial coding of the beams.

2. Design

2.1 Device Components

The structure of the silicon photonics integrated device is shown in Fig. 1. The left-most end of the device is the input coupler whose function is to couple the input light from fiber into waveguide on device. Then the light enters into three-stage cascaded MZIs. Electrodes are applied to the upper arm of each stage of MZI, which is a 2 μm-wide and 140 μm-long resistive TiN wire. When a voltage is applied to the wires, heat is generated and the refractive index of upper arm is changed, the phase of MZIs' response curve changes accordingly. The output ports of cascaded MZIs are also marked in Fig. 1. Light with the same wavelength as the resonant peak of micro-ring enters the corresponding emitter from the drop end of the micro-ring. And then it is emitted into free space. Light of other wavelengths still travels forward, repeating the previous process to the next micro-ring. The optical scanners which use MZIs or micro-ring as optical switches and use lens to control the beam direction have been demonstrated many times in recent years [19]–[21].

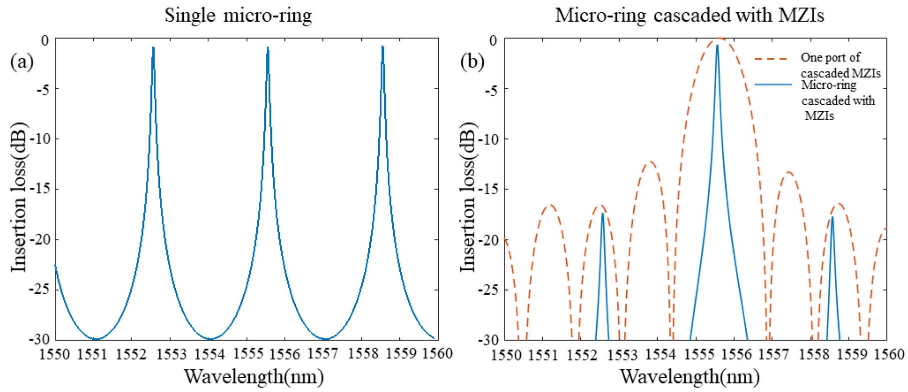

Fig. 2. (a) Simulated result of a single micro-ring. (b) Simulated result of micro-ring cascaded with MZIs.

2.1.1 Filter Module: Filter module is used for wavelength division. Three-stage cascaded MZIs and array of micro-rings are combined to achieve filtering process. The free spectral range (FSR) of the first, second and third stage MZI are set to be 2.5 nm, 5 nm and 10 nm respectively. After MZI chain there are eight output ports, 3 dB bandwidth of each port is 1.25 nm and each output port is followed by eight cascaded micro-rings whose resonant wavelengths are all different. Thus a total of 64 micro-rings are placed on the device, they are arranged into an 8×8 rectangular array. Through the filter module, 64 light beams with different wavelengths are emitted from different positions on the device.

One characteristic of this structure is to relax the precision of the micro-ring fabrication process. It is known that the process error will have greater influence when the ring radius gets smaller. The relationship between the wavelength error of resonant peak and the processing error is as follows.

$$\Delta\lambda = \lambda\left(\frac{\Delta R}{R} + \frac{\Delta n}{n} + \frac{\Delta R * \Delta n}{n * R}\right) \tag{1}$$

$\Delta\lambda$ is the deviation of the resonant wavelength of micro-ring, λ is the resonant wavelength, R is the radius of micro-ring and ΔR is the error of radius, n is the effective refractive index of waveguide and Δn is its error. It can be seen from the formula that when the process error ΔR is determined, the larger the radius R of the micro-ring, the smaller the deviation $\Delta\lambda$ of the resonant peak.

In our design, the FSR of the micro-ring can be a little bit larger than the bandwidth of the cascaded MZI output (1.25 nm), instead of greater than the entire 10nm wavelength range, which can greatly increase the radius of the micro-ring. The difference in the resonant wavelength between adjacent micro-rings in one MZI output port is set to be 0.16 nm, which will be slightly different from the design value because of the existence of processing error.

The waveguide on the device is 450 nm wide and 220 nm high, the group refractive index of the waveguide is about 4.26 at 1550 nm and the effective refractive index is about 2.33. Thus it can be calculated that the length difference of the two MZI arms ΔL of the first stage MZI is 225.6 μm, the ΔL of the second stage MZI is 112.8 μm, and the ΔL of the third stage MZI is 56.4 μm, Electrodes are fabricated on MZI upper arm waveguide. By adding voltage to the electrodes, we can heat the waveguide and change the phase.

The radius of the micro-rings is about 30 μm. The spacing between the ring waveguide and the straight waveguide is set to be 300 nm. According to the simulation results by FDTD, the 3dB bandwidth of the micro-ring can reach 0.1 nm in this case, Fig. 2(a) shows the simulated result of a single micro-ring, and Fig. 2(b) shows the simulated result after the micro-ring is cascaded with three-stage cascaded MZIs. It's shown that the FSR of single micro-ring is enlarged and only one resonant peak lives in 10 nm bandwidth.

2.1.2 Design of Emitter Array: The fan shaped gratings are used as the optical emitter with a period of 625 nm, a duty cycle of 50%, and an etch depth of 70 nm. With regard to the coupling

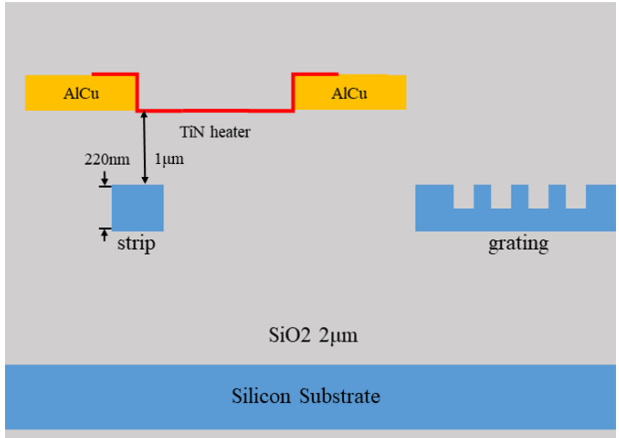

Fig. 3. Layer structure of silicon photonic integrated device.

efficiency of gratings, it can be obtained that the emission efficiency of gratings is 44.67% by FDTD simulation, the coupling efficiency here refers to the ratio of the light power emitted out from the grating to the input light power. The average FWHM spot size of the emitter is about 10 microns. The emitter array consists of 64 such gratings which are arranged into 8 $\times$ 8 rectangular array. The transverse and longitudinal space between adjacent emitters are 100 μm and 150 μm respectively. Theoretically, as long as space permits, the emitter array can be arranged in any desired shape, thus the output beams can also be scanned with any shape for different applications.

2.2 Device Structure

2.2.1 Layer Structure: The SOI device is fabricated using IMECAS's wafer fabrication platform, a cross-section of the layer structure of silicon photonic integrated device is shown in Fig. 3. The bottom layer of the device is the silicon substrate. A 2 μm-thickness layer of SiO_2 is deposited on the silicon substrate. Above it is a 220 nm-thickness layer of silicon, waveguide and gratings are formed in this layer. The waveguide has a width of 450 nm and a height of 220 nm. There is a layer of SiO_2 with a thickness of 1 μm on top of the patterned silicon layer. Heater electrodes are formed in a thin film of TiN deposited on top of the SiO_2 layer. The pads and wiring lines are formed in AlCu deposited on the heater electrodes.

2.2.2 Device Package: The packaged device is shown in Fig. 4. A fiber is attached to the input coupler of device, and the device is mounted on a printed circuit board which gold wires are attached on. Needle array is used to connect printed circuit board to the voltage control circuit to adjust the phase of each MZI. Device lies on a copper substrate, bonded together with silver paste. A thermoelectric cooler (TEC) is lined under the copper substrate to give feedback to the temperature change of the device, so that the temperature of the device remains basically the same. The main source that makes device temperature change is the heater on the MZI, which leads to change in refractive index and characteristics of the structure. The packaged device is small and easy to transfer, its placement can be changed according to the specific application scenario and environment.

3. Experimental Results

3.1 Filtering Results

The responses of each stage of MZI and one output port of cascaded MZIs are shown in Fig. 5(a)–(d). Port1 and port2 in the figure represent the two output ports of MZI. Port1 refers

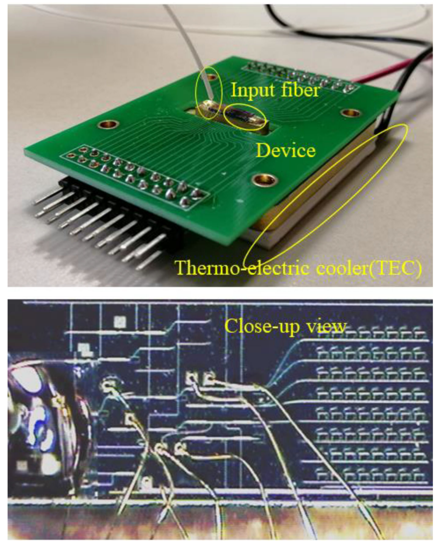

Fig. 4. Picture of packaged device.

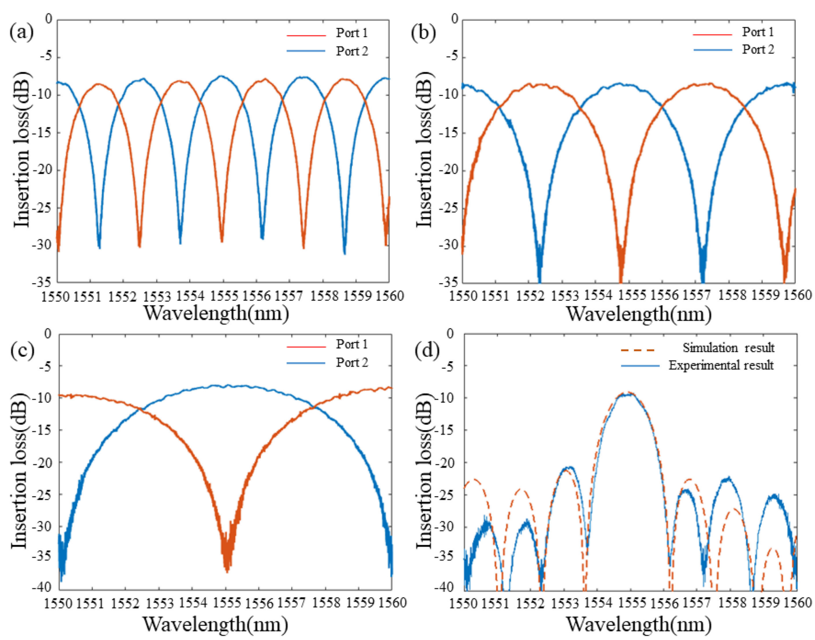

Fig. 5. Experimental response of each stage of MZI and the response of one output port of cascaded MZIs. (a) First-stage MZI. (b) Second-stage MZI. (c) Third-stage MZI. (d) One output port of cascaded MZIs

to the upper port, and port2 refers to the lower port. It can be seen that the spectrum of cascaded MZIs fits well with the design.

Response curves of micro-rings are shown in Fig. 6(a). The transmission spectrum is on the drop port of the ring. It can be seen from the results that the 3dB bandwidth of each micro-ring is about 0.1 nm, resonant peaks of 64 micro-rings are staggered in the wavelength range of 10 nm. The average Q of the micro-rings is 1.93×10^4 and the average FSR of the micro-rings is 3.05 nm. The corresponding relationship between wavelength and ports of cascaded MZIs is shown in Fig. 6(b). In order to describe the performance of the device more clearly, the resonant wavelength and insertion loss of 64 resonant peaks are listed in Table 1, and the channel isolation of scanning is

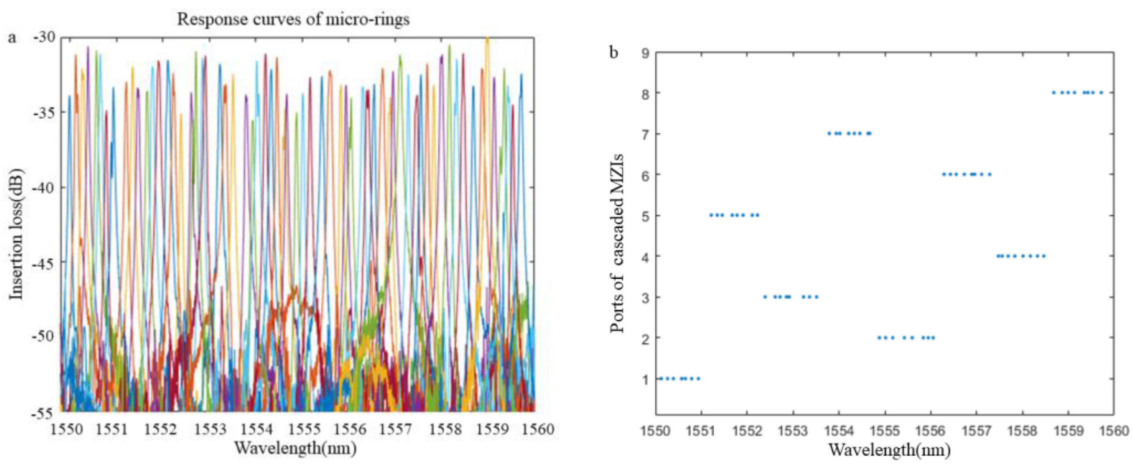

Fig. 6. (a) Measured spectrum curves of 64 micro-rings. (b) Wavelength for each port of cascaded MZIs.

TABLE 1
Resonant Peak Wavelength and Insertion Loss

row \ column	1	2	3	4	5	6	7	8
1	1549.99nm\ -34.4dB	1550.13nm\ -31.7dB	1550.27nm\ -32.6dB	1550.39nm\ -31.1dB	1550.57nm\ -31.4dB	1550.66nm\ -31.6dB	1550.79nm\ -35.4dB	1550.94nm\ -33.8dB
2	1554.88nm\ -35.5dB	1555.02nm\ -34.2dB	1555.17nm\ -33.2dB	1555.42nm\ -33.1dB	1555.6nm\ -32.7dB	1555.84nm\ -33.7dB	1555.94nm\ -33.7dB	1556.05nm\ -34.5dB
3	1552.39nm\ -35.6dB	1552.61nm\ -34.2dB	1552.72nm\ -31.5dB	1552.85nm\ -31.9dB	1552.92nm\ -31.7dB	1553.23nm\ -32.3dB	1553.36nm\ -33.6dB	1553.51nm\ -33dB
4	1557.48nm\ -34.4dB	1557.56nm\ -33dB	1557.69nm\ -32.3dB	1557.83nm\ -33.7dB	1558.01nm\ -31.7dB	1558.17nm\ -31dB	1558.33nm\ -31.9dB	1558.46nm\ -31.6dB
5	1551.22nm\ -33.5dB	1551.35nm\ -32.5dB	1551.46nm\ -33.9dB	1551.67nm\ -34.1dB	1551.78nm\ -32.4dB	1551.91nm\ -32.1dB	1552.11nm\ -32dB	1552.22nm\ -32.9dB
6	1556.29nm\ -33.8dB	1556.43nm\ -34dB	1556.55nm\ -33.6dB	1556.73nm\ -32.6dB	1556.89nm\ -34.5dB	1556.96nm\ -32.8dB	1557.11nm\ -31.7dB	1557.29nm\ -33dB
7	1553.79nm\ -34.3dB	1553.94nm\ -35.7dB	1554.02nm\ -32.1dB	1554.21nm\ -31.6dB	1554.34nm\ -32.6dB	1554.46nm\ -31.8dB	1554.63nm\ -35.3dB	1554.67nm\ -34.3dB
8	1558.68nm\ -33.7dB	1558.87nm\ -32.6dB	1558.99nm\ -30dB	1559.13nm\ -33.2dB	1559.35nm\ -32.6dB	1559.43nm\ -33.7dB	1559.53nm\ -35dB	1559.72nm\ -32.9dB

TABLE 2
Channel Isolation

row \ column	1	2	3	4	5	6	7	8
1	12.8dB	18.2dB	10.0dB	11.6dB	10.7dB	11.1dB	10.1dB	16.1dB
2	12.3dB	14.4dB	15.0dB	13.2dB	15.3dB	15.3dB	12.4dB	13.6dB
3	13.8dB	8.5dB	13.7dB	7.1dB	10.8dB	10.9dB	12.0dB	18.2dB
4	11.5dB	11.2dB	14.4dB	14.0dB	15.7dB	16.4dB	15.1dB	14.8dB
5	13.1dB	13.9dB	12.3dB	11.2dB	13.3dB	13.6dB	13.8dB	11.0dB
6	13.4dB	12.3dB	12.2dB	15.4dB	7.4dB	10.3dB	17.0dB	11.4dB
7	16.2dB	7.5dB	12.1dB	15.3dB	14.1dB	15.8dB	2.8dB	6.3dB
8	17.0dB	12.3dB	13.8dB	14.0dB	11.0dB	10.8dB	10.5dB	17.2dB

listed in Table 2. The rows and columns in the tables correspond to the rows and columns of the micro-rings array in Fig. 1. The number increases from left to right and from top to bottom. The order of ports is arranged from top to bottom according to the layout. The power required to tune the MZI heaters are listed in Fig. 7. The total electric power applied on the device is about 174 mw.

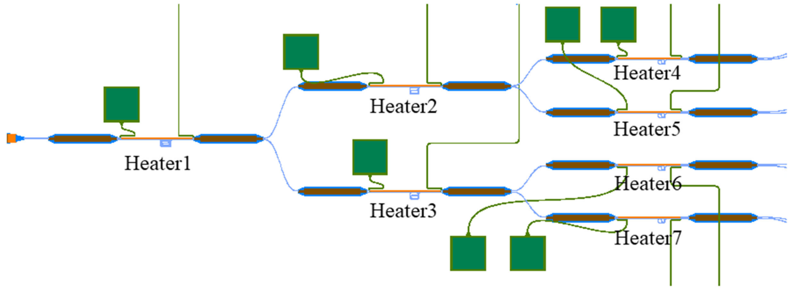

Heater number	1	2	3	4	5	6	7
Voltage	5.53 V	3.55 V	6.1 V	8.95 V	8.2 V	8.35 V	6.55 V
Power	15.29 mw	6.36 mw	16.91 mw	44.5 mw	35.39 mw	34.86 mw	20.43 mw

Fig. 7. The power required to tune the MZI heaters.

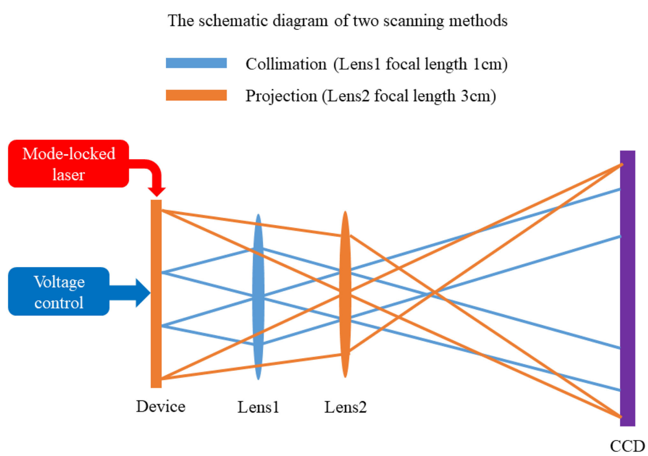

Fig. 8. The schematic diagram of two scanning methods.

3.2 Scanning Results

Two types of working mode (collimation and projection) were tested by locating the lenses at different positions, as shown in Fig. 8. The pixel array of the infrared CCD is 640 $\times$ 512, and the size of each pixel is 20 μm, so its photosensitive area is 1.28 $\times$ 1.02 cm^2. A mode-locked laser with center wavelength 1555nm and bandwidth larger than 15nm is used as the light source. Collimation is achieved by setting the distance between the lens and the chip equal to the focal length. In this case, the light beams emitted from the device become collimated beams after passing through the lens, which can be used for scanning large depth of field, for example, Lidar or optical wireless communications [22], [23]. Range of scanning angle is determined by the position of the emitter with respect to the optic axis of the lens and the focal length of the lens. The other way to achieve scanning is projection, small light spots appear in image plane of the system and then the beam continues to diverge after passing through the image plane, which makes it suitable for applications with small depth of field but high scanning resolution like laser imaging.

3.2.1 Collimation: In order to obtain a larger scanning angle, a lens with 1cm focal length is chosen and the distance between lens and device is set to 1cm too. As mentioned above, beams are collimated after passing through the lens, so the divergence angle is quite small and the size of beams can be sustained for a long distance. Distribution of beams collected by an infrared CCD (Bobcat-640-CL manufactured by xenics) at a distance of 10 cm from lens is shown in Fig. 9. The FWHM spot size of the beam is about 0.32 degrees and the space between nearby beams in θ and

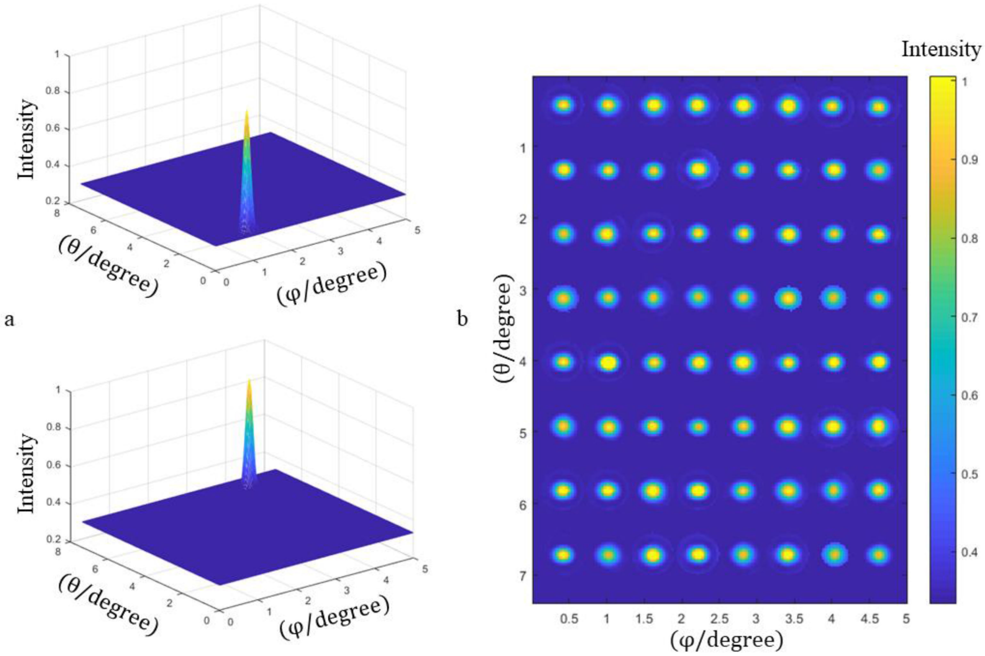

Fig. 9. (a) Distribution of light beams pointing in two different directions. (b) Scanning lattice received by infrared CCD in collimation scanning.

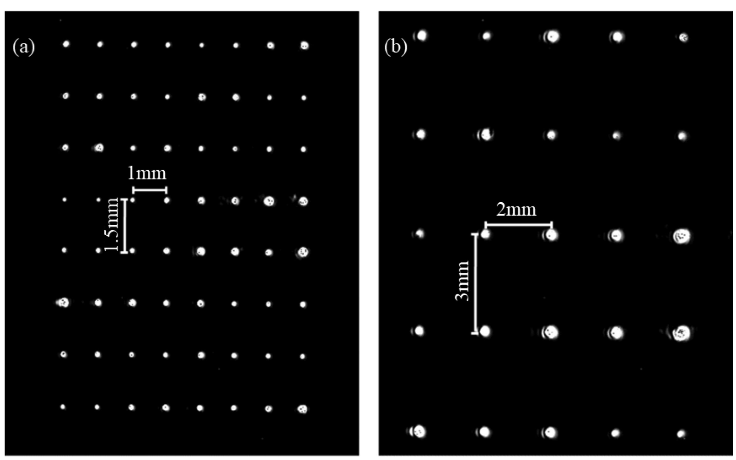

Fig. 10. Scanning lattice received by infrared CCD in projection mode. (a) 10 times magnification (b) 20 times magnification.

φ direction are 0.57 degrees and 0.86 degrees. The divergence angle of each beam is 0.1° and the range of scanning angle is 6° $\times$ 4° in such case.

3.2.2 Projection: Firstly, lens with a focal length of 3 cm is placed 3.3 cm away from the device, the infrared CCD is placed on the image plane of the system. In this case, the magnification rate is 10. As shown in Fig. 10(a), the lateral distance between the spots is 1 mm and the longitudinal distance is 1.5 mm. an area of 8 mm x 10.5 mm can be covered by spots array. 20 times magnification is also tested by locating the lens at a distance of 3.15 cm from the device, the lateral distance between the spots become 2 mm and the longitudinal distance become 3 mm this time. The size of the entire array has exceeded the photosensitive area of the CCD, so only a part of the spots array can be seen on CCD, as shown in Fig. 10(b).

4. Summary and Conclusion

A 2D wavelength-scanning device based on silicon photonic integrated technology is proposed and demonstrated. This kind of wavelength-to-space mapping device can realize 2D high-speed scanning simply by changing the input wavelength. Filter module and emitter array are two main parts of the device. The rate of scanning can be variable from kilo-Hz to Mega-Hz by wavelength scanning lasers [24], [25] or time-stretch technologies [26], [27]. However, traditional tunable lasers have complex structures and high cost. In contrast, integrated wavelength-tuned lasers will be a better choice [28]–[30]. They are small in size, simple in structure and can be integrated with our device. The range of scanning angle and scanning resolution can also be adjusted by the parameters of lens system used. In addition, the device is also easy to operate and small in size. At present, this device is processed on SOI platform and can only obtain 64 scanning points. The number of scanning points is mainly limited by the effect of filtering, to obtain more scanning points, the resonant peak bandwidth of the micro-ring needs to be narrower. However, as mentioned above, due to the existence of processing error, narrow bandwidth will lead to the splitting of resonant peaks. Compared to the silicon waveguide, the refractive index difference between the core layer and the cladding layer in silicon nitride waveguide is smaller, therefore, its turning radius is larger, which means the processing error has less influence on the result. A narrower bandwidth of resonant peak can be achieved with silicon nitride platform, thus more scanning points can be obtained, which can greatly improve the performance. This is the next part of our future work. To sum up, this integrated wavelength-space distribution device has a promising prospect to play important roles in many applications, such as Lidar, optical wireless communication and ultra-high-speed imaging.

Acknowledgment

The authors declare that there are no conflicts of interest related to this article.

References

[1] G. Wang *et al.*, “Highly efficient optical beam steering using an in-fiber diffraction grating for full duplex indoor optical wireless communication,” *J. Lightw. Technol.*, vol. 36, no. 19, pp. 4618–4625, Oct. 2018.
[2] D. C. O’Brien, “Beamsteering for ultra-high data-rate optical wireless communications,” in *Proc. Broadband Access Commun. Technologies XIII*, vol. 10945. International Society for Optics and Photonics, 2019.
[3] F. Guidi, “Indoor environment-adaptive mapping with beamsteering massive arrays,” *IEEE Trans. Veh. Technol.*, vol. 67, no. 10, pp. 10139–10143, Oct. 2018.
[4] O. Mattausch and O. Goksel, “Image-based reconstruction of tissue scatterers using beam steering for ultrasound simulation,” *IEEE Trans. Med. Imag*, vol. 37, no. 3, pp. 767–780, Mar. 2018.
[5] T. A. Heinz, “Shear motor for dynamic mount for laser-beam steering mirror,” U.S. Patent 4,775,815, Oct. 4, 1988.
[6] Z. Zhou, B. Yin, and J. Michel, “On-chip light sources for silicon photonics,” *Light Sci. Appl.*, vol. 4, no. 11, p. e358, 2015.
[7] J. K. Doylend, “Two-dimensional free-space beam steering with an optical phased array on silicon-on-insulator,” *Opt. Exp.*, vol. 19, no. 22, pp. 21595–21604, 2011.
[8] C. V. Poulton, “Coherent solid-state LIDAR with silicon photonic optical phased arrays,” *Opt. Exp.*, vol. 42, no. 20, pp. 4091–4094, 2017.
[9] R. Blanchard, “Modeling nanoscale V-shaped antennas for the design of optical phased arrays,” *Phys. Rev. B*, vol. 85, no. 15, 2012, Art. no. 155457.
[10] K. Van Acoleyen, H. Rogier, and R. Baets, “Two-dimensional optical phased array antenna on silicon-on-insulator,” *Opt. Exp.*, vol. 18, no. 13, pp. 13655–13660, 2010.
[11] D. Kwong, “On-chip silicon optical phased array for two-dimensional beam steering,” *Opt. Lett.*, vol. 39, no. 4, pp. 941–944, 2014.
[12] D. Kwong, “1 $\times$ 12 Unequally spaced waveguide array for actively tuned optical phased array on a silicon nanomembrane,” *Appl. Phys. Lett.*, vol. 99, no. 5, 2011, Art. no. 051104.
[13] A. Yaacobi, “Integrated phased array for wide-angle beam steering,” *Opt. Lett.*, vol. 39, no. 15, pp. 4575–4578, 2014.
[14] K. Van Acoleyen, “One-dimensional off-chip beam steering and shaping using optical phased arrays on silicon-on-insulator,” *J. Lightw. Technol.*, vol. 29, no. 23, pp. 3500–3505, Dec. 2011.
[15] J. Sun, “Large-scale nanophotonic phased array,” *Nature*, vol. 493, no. 7431, p. 195, 2013.

[16] Y. Zhang, "Sub-wavelength-pitch silicon-photonic optical phased array for large field-of-regard coherent optical beam steering," *Opt. Exp.*, vol. 27, no. 3, pp. 1929–1940, 2019.
[17] S. W. Chung, H. Abediasl, and H. Hashemi, "A monolithically integrated large-scale optical phased array in silicon-on-insulator CMOS," *IEEE J. Solid-State Circuits*, vol. 53, no. 1, pp. 275–296, Jan. 2018.
[18] B. Zhang, "Serpentine optical phased array silicon photonic aperture tile with two-dimensional wavelength beam steering," in *Proc. Opt. Fiber Commun. Conf.*, Optical Society of America, 2019, paper M4E5.
[19] Y. C. Chang, M. C. Shin, and C. T. Phare, "Metalens-enabled low-power solid-state 2D beam steering," in *Proc. Conf. Lasers Electro-Optics Sci. Innov.*, Optical Society of America, 2019, paper SF3N. 5.
[20] J. J. López, "Planar-lens enabled beam steering for chip-scale LIDAR," in *Proc. Conf. Lasers Electro-Optics*, IEEE, 2018.
[21] D. Inoue, "Demonstration of a new optical scanner using silicon photonics integrated circuit," *Opt. Exp.*, vol. 27, no. 3, pp. 2499–2508, 2019.
[22] T. Koonen, "Ultra-high capacity indoor optical wireless communication using 2D-steered pencil beams," *J. Lightw. Technol.*, vol. 34, no. 20, pp. 4802–4809, Oct. 2016.
[23] C. W. Oh, E. Tangdiongga, and A. M. J. Koonen, "42.8 Gbit/s indoor optical wireless communication with 2-dimensional optical beam-steering," in *Proc. Opt. Fiber Commun. Conf. Exhib.*, IEEE, 2015.
[24] M. Oberg, "A three-electrode distributed Bragg reflector laser with 22 nm wavelength tuning range," *IEEE Photon. Technol. Lett.*, vol. 3, no. 4, pp. 299–301, Apr. 1991.
[25] S. Yamashita and Y. Takubo, "Wide and fast wavelength-swept fiber lasers based on dispersion tuning and their application to optical coherence tomography," *Photon. Sens.*, vol. 3, no. 4, pp. 320–331, 2013.
[26] F. Coppinger, A. S. Bhushan, and B. Jalali, "Photonic time stretch and its application to analog-to-digital conversion," *IEEE Trans. Microw. Theory Techn.*, vol. 47, no. 7, pp. 1309–1314, Jul. 1999.
[27] A. Mahjoubfar, "Time stretch and its applications," *Nature Photon.*, vol. 11, no. 6, p. 341, 2017.
[28] M. A. Tran, "A widely-tunable high-SMSR narrow-linewidth laser heterogeneously integrated on silicon," in *Proc. Conf. Lasers Electro-Optics Appl. Technol.*, Optical Society of America, 2018.
[29] T. Komljenovic, "Control of widely tunable lasers with high-Q resonator as an integral part of the cavity," *J. Lightw. Technol.*, vol. 35, no. 18, pp. 3934–3939, Sep. 2017.
[30] N. Li, "Monolithically integrated erbium-doped tunable laser on a CMOS-compatible silicon photonics platform," *Opt. Exp.*, vol. 26, no. 13, pp. 16200–16211, 2018.